

Effect of Tundish Impact Zone Optimization on Inclusion Removal in Steel: Industrial and Simulation Studies



JIN WANG, WEI LIU, SHUFENG YANG, XIAOTAN ZUO, LI ZHAO, and JINGSHE LI

This study provided comprehensive insights into designing and optimizing tundishes. A tundish is a fundamental reactor contributing to the metallurgical process. This reactor acts as a critical stabilizer of the molten steel flow field, and it facilitates the removal of inclusions by floatation. Numerical simulations, physical experiments, and industrial trials were systematically performed to validate a two-step optimization approach based on the tundish impact zone volume. The two-step approach was shown to facilitate the rapid preliminary optimization of the tundish. The excellent impact zone volume ratio of 19.3 pct was verified. After optimization, there was a decrease in the stagnant zone in the tundish from 22.92 to 16.27 pct relative to the primary design. Furthermore, there was a noteworthy reduction in the total mass of inclusions (TMIs) during different casting periods, as demonstrated by billet sample findings from electrolytic weighing. There was a notable reduction in the TMIs for strand 1 and strand 3 from 2.46 and 2.52 mg/10 kg to 1.06 and 1.68 mg/10 kg, respectively, at the intermediate heat, indicating an improvement in inclusion removal efficiency. The causes of cracking in the retaining walls were investigated, including the variation in cracking risk for multiposition retaining walls.

<https://doi.org/10.1007/s11663-024-02994-7>

© The Minerals, Metals & Materials Society and ASM International 2024

I. INTRODUCTION

THE removal and modification of inclusions in steel have garnered significant attention in recent years.^[1–3] It is known that molten steel and inclusions in the liquid smelting process possess favorable physical and chemical properties, and effective measures can be employed to control them. Among the reactors in the metallurgical production process, tundishes are exceptionally critical.^[4] As a liquid reaction vessel, the flow state within a tundish significantly influences the removal of inclusions and the homogenization of alloy components. Hence, numerous scholars have focused on optimizing and

enhancing the performance of basic flow control components, such as perforated retaining walls,^[5,6] weirs and dams,^[7] and turbulence suppressors,^[8] to investigate their impacts on the flow field.

The control of the flow field in the tundish is crucial for improving the removal rate of inclusions. Inclusions in steel have detrimental effects on key indicators, such as corrosion resistance,^[9,10] fatigue life,^[11,12] and tensile strength.^[13] Furthermore, inclusions can disrupt the normal production process, as exemplified by aluminum oxide inclusions, which frequently obstruct the water outlet during the smelting process.^[14] Due to limited operability in industrial sites, researchers rely on modeling to evaluate the inclusion removal rate.^[15–18] Among numerical models, the Euler–Lagrange method is widely used, where the transient flow of steel is determined by solving the Navier–Stokes equation within the Euler framework, and the motion of inclusions is tracked within the Lagrange framework. Inclusions are introduced as particles at the inlet, and the proportion of inclusions trapped by the slag layer over a specific period is used to evaluate the removal efficiency. Although these removal rates generally capture trends well, the differences in capture criteria significantly affect the actual behaviors of inclusions. Yao *et al.*^[15] established a new inclusion capture criterion that exhibits good agreement with experimental data, challenging the previous standard that yield high removal rates. Liu

JIN WANG, WEI LIU, and JINGSHE LI are with the School of Metallurgical and Ecological Engineering, University of Science and Technology Beijing, Beijing 100083, P.R. China. Contact e-mail: liuwei@ustb.edu.cn SHUFENG YANG is with the School of Metallurgical and Ecological Engineering, University of Science and Technology Beijing and also with the State Key Laboratory of Advanced Metallurgy, University of Science and Technology Beijing, Beijing 100083, P.R. China. Contact e-mail: yangshufeng@ustb.edu.cn XIAOTAN ZUO and LI ZHAO are with the Wuhu Xinxing Ductile Pipe Co., Ltd., Wuhu 241002, Anhui, P.R. China.

Manuscript submitted September 4, 2023; accepted December 24, 2023.

Article published online February 5, 2024.

et al.^[19] developed a computational fluid dynamics (CFD) model incorporating the phase field and fluid–structure interaction (FSI) approaches to simulate the floating behaviors of solid inclusions in steel and their interactions with the steel–slag interface, providing detailed insights into inclusion behavior. Ding *et al.*^[18] discovered a linear relationship between the inclusion removal rate, inclusion radius, and specific parameters, such as minimum residence time, peak concentration time, and average residence time. In this work, we conducted industrial experiments to measure the total mass of inclusions (TMIs) in the cast billet instead of relying on a mathematical model to assess the inclusion removal capacity of the tundish.

In addition to the removal of inclusions, the flow state of molten steel in the tundish is evaluated using the combined model theory proposed by Sahai,^[20] which has been widely employed in numerical and physical simulations. Slow-flowing areas in the molten steel are identified as stagnant zones, and the calculation of these areas is influenced by the computational model. The validity of the model necessitates a comparison of results from mathematical and physical simulations. Yang *et al.*^[21] established a residence time distribution (RTD) model to investigate the flow characteristics of molten steel in a channel-type induction heating tundish. Su *et al.*^[22] proposed a new theoretical framework that divides the well-mixed volume into equivalent volume, active volume, and dead mixing volume, allowing the calculation of the stagnant zone.

The optimization of the tundish is a prerequisite for performance evaluation. Previously, scholars did not focus much on the influence of the impact zone volume on the overall metallurgical performance of the tundish. Instead, the researchers primarily conducted independent and semi-independent analyses of basic flow control components and impact zones. In practice, the tundish is constructed with multiple structures, and optimal performance is hindered by a lack of clear optimization guidelines. We proposed a two-step optimization approach based on the volume of the tundish impact zone to fill this gap. The two-step optimization concept was methodically and extensively executed and confirmed through numerical simulations, physical simulations, and industrial trials. The results obtained from the industrial trials and simulations provide accurate and quantitative information about important metallurgical properties, such as the inclusion removal efficiency and flow field uniformity, for the optimized tundish structure.

II. EXPERIMENT AND ANALYSIS METHODS

A. Geometric Structure of the Tundish

We focused on a specialized tundish for continuous casting within a manufacturing plant. The tundish is segmented into casting and impact areas, and the major components of the tundish are the ladle shroud, retaining wall, diversion hole, stopper rod, and turbulent suppressor. Figure 1(a) displays the top view of the tundish, measuring 4795 mm in length and 2120 mm in width. Figure 1(b) illustrates the tundish geometry and

impact zone prior to industrial trials. The three outlets were named strands 1, 2, and 3 based on the outlet spacing (1800 mm) shown in Figure 1(a). These dimensional parameters support the simulation experiment and the establishment of the tundish model, which is the initial step of the simulation.

B. Numerical Simulation

The numerical simulation was implemented by the CFD software ANSYS Fluent, and the coupling of the pressure and velocity fields was calculated using SIMPLE algorithms. The temperature field change was taken into account, the molten steel inlet temperature was set to 1873 K, and the physical and simulated operating parameters of the molten steel specimens are shown in Table I.

1. Main assumptions and considerations

The tundish casting process is a high-temperature black box model. Existing basic research cannot accurately describe the flow of molten steel in a tundish; thus, the calculation needs to be constrained, and the necessary assumptions are as follows:

- (1) The fluid in the tundish is regarded as a Newtonian incompressible fluid, and the flow state is regarded as a three-dimensional steady-state flow.
- (2) The interface between the fluid and the tundish lumen is set to a slip-free boundary; that is, the velocity on the inner wall of the tundish is 0.
- (3) The physical parameters used in the numerical simulation are regarded as constants and do not change with fluid temperature fluctuations.
- (4) The liquid level of tundish steel–slag has no shear force, and the flow of molten steel and the removal of inclusions are affected by the physical properties of the slag layer.

2. Basic governing equations

Fluid flow is described by the continuity equation and the momentum equation of the Euler–Lagrange method (Navier–Stokes equation):

$$\frac{\partial(\rho u_i)}{\partial x_i} = 0, \quad [1]$$

$$\frac{\partial(\rho u_i)}{\partial t} + \frac{\partial(\rho u_i u_j)}{\partial x_j} = \frac{\partial}{\partial x_i} \left[\mu_{\text{eff}} \left(\frac{\partial u_i}{\partial x_j} + \frac{\partial u_j}{\partial x_i} \right) \right] - \frac{\partial P}{\partial x_i} + \rho g_i, \quad [2]$$

where ρ is the density of molten steel (kg/m^3); u is the fluid velocity (m/s); t is the time (s); subscripts i and j are the coordinate components; $\mu_{\text{eff}} = \mu + u_t$, where μ_{eff} is the effective viscosity (Pa s), μ is the dynamic viscosity (Pa s), u_t is the turbulent viscosity (Pa s), g_i is the acceleration of gravity (m/s^2), and P is the pressure (Pa).

The simulation process used the $\kappa - \varepsilon$ model to calculate the turbulent kinetic energy and turbulent energy dissipation rate of the fluid:

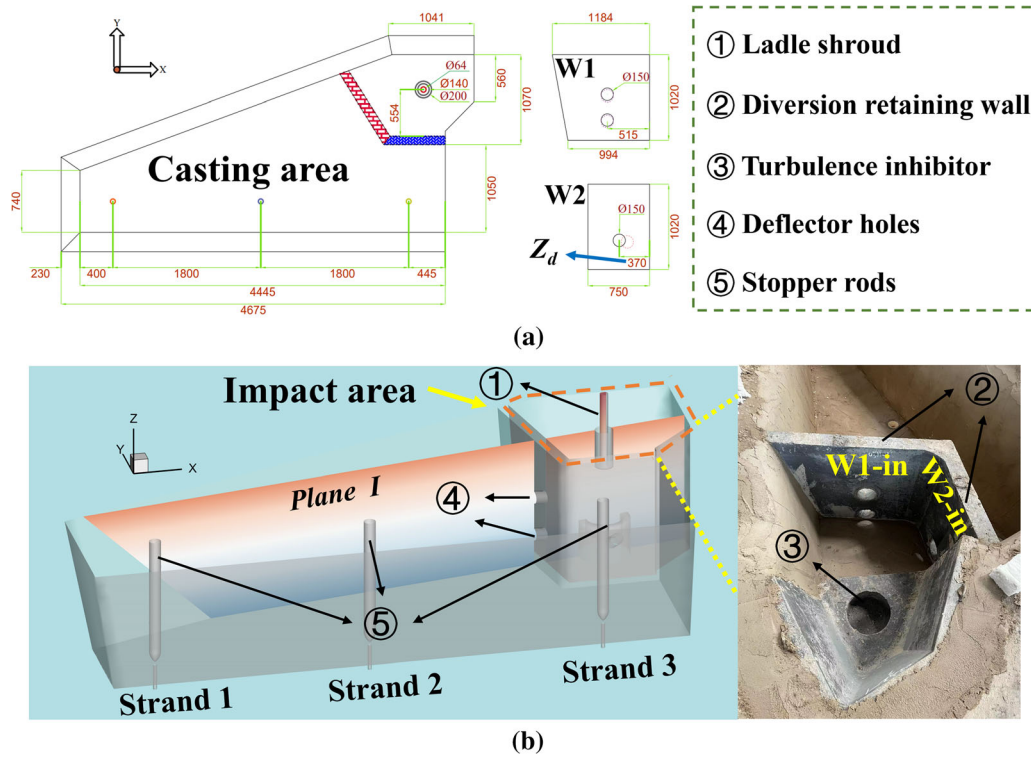


Fig. 1—Schematic diagram of the tundish structure and size parameters: (a) top view and (b) schematic structure.

Table I. Numerical Simulation Parameters

Parameters	Value	Parameters	Value
Working Height of Tundish	1020 (mm)	heat capacity	750 (J/kg·K)
Diameter of the Ladle Shroud	64 (mm)	thermal conductivity	41 (W/m·K)
Diameter of the Outlet	30 (mm)	viscosity	6.1×10^{-3} (kg/m s)
Submergence Depth of Ladle Shroud	300 (mm)	inlet turbulent energy dissipation rate	8.8×10^{-4} (m^2/s^3)
Distance Between Two Outlets	1800 (mm)	inlet turbulent energy	1.47×10^{-3} (m^2/s^2)
Inlet Velocity	0.869 (m/s)	density of liquid steel	6800 (kg/m^3)
Bottom Wall Heat Flux	- 1800 (W/m^2)	walls heat flux	- 4000 (W/m^2)
Top Wall Heat Flux	- 15000 (W/m^2)		

$$\frac{\partial(\rho u_i \kappa)}{\partial x_i} = \frac{\partial}{\partial x_i} \left[\left(\mu_{\text{eff}} + \frac{u_t}{\sigma_\varepsilon} \right) \frac{\partial \kappa}{\partial x_i} \right] + G - \rho \varepsilon, \quad [3]$$

$$\frac{\partial(\rho u_i c_p T)}{\partial x_i} = \frac{\partial}{\partial x_i} \left(k_{\text{eff}} \frac{\partial T}{\partial x_i} \right), \quad [5]$$

$$\frac{\partial(\rho u_i \varepsilon)}{\partial x_i} = \frac{\partial}{\partial x_i} \left[\left(\mu_{\text{eff}} + \frac{u_t}{\sigma_\varepsilon} \right) \frac{\partial \varepsilon}{\partial x_i} \right] + \frac{c_1 \varepsilon G - c_2 \rho \varepsilon^2}{\kappa}, \quad [4]$$

where $G = u_t \frac{\partial u_i}{\partial x_i} \left(\frac{\partial u_i}{\partial x_j} + \frac{\partial u_j}{\partial x_i} \right)$; $u_t = c_u \rho \frac{\kappa^2}{\varepsilon}$, where u_t is the additional viscosity coefficient of the fluid ($\text{kg}/\text{m}\cdot\text{s}$); k is the turbulent kinetic energy (m^2/s^2); ε is the dispersion rate of turbulent energy consumption (m^2/s^3); and c_1 , c_2 , c_u , σ_κ , and σ_ε are empirical constants set to the recommended Launder values^[23]: $c_1 = 1.43$, $c_2 = 1.92$, $c_u = 0.09$, and $\sigma_\kappa = 1$; $\sigma_\varepsilon = 1.3$.

The energy equation was used to observe the temperature changes between different models during the flow of molten steel:

where c_p is the specific heat capacity of molten steel ($\text{J}/\text{kg}\cdot\text{K}$); T is the temperature of molten steel (K); and k_{eff} is the effective heat transfer coefficient ($\text{W}/\text{m}^2\cdot\text{K}$).

3. Tracer transport equation

The RTD curve of the tundish outlet was monitored by adding tracer to the molten steel, and the flow state of the molten steel was described mathematically:

$$\rho \frac{\partial c}{\partial t} + \rho u_i \frac{\partial c}{\partial x_i} = \frac{\partial}{\partial x_i} \left(\rho D_{\text{eff}} \frac{\partial c}{\partial x_i} \right), \quad [6]$$

where D_{eff} is the effective kinematic diffusivity, and $D_{\text{eff}} = D_0 + \frac{\mu_{\text{eff}}}{\rho S c_t}$; c is the dimensionless concentration for tracer; $S c_t$ is the turbulent Schmitt number equal to 0.7; and D_0 is the tracer diffusion coefficient (m^2/s) equal to 2.88×10^{-5} .

4. RTD curve calculation model

RTD curve calculations describe the sizes of the stagnant zones in the tundish.^[20] For the theoretical average residence time (τ) of the tundish, the average residence time of a single strand (t_m) and the overall average residence time (t_a) were calculated by Eqs. [7 through 9], respectively:

$$\tau = \frac{V}{Q} \quad [7]$$

$$t_m = \frac{\sum t_n c_n \Delta t_n}{\sum c_n \Delta t_n} \quad [8]$$

$$t_a = \frac{1}{N} \sum_{m=1}^N t_m, \quad [9]$$

where Q is the volume flow rate (m^3/s); V is the tundish volume (m^3); subscripts m and n represent the tundish strand and moment, respectively; Δt_n is the monitoring interval; and N is the number of tundish casting strands.

The transformation formulas for dimensionless time (θ) and dimensionless tracer concentration ($E_m(\theta)$) at the n moment of the m strand of the tundish are Eqs. [10] and [11],^[24] respectively:

$$\theta = \frac{t_n}{\tau} \quad [10]$$

$$E_m(\theta) = \frac{1}{N} \alpha \tau c_m(t_n), \quad [11]$$

where $\alpha = \frac{N c_0 \Delta t'}{\sum_{m=1}^N \sum_{n=0}^{\infty} c_m(t_n) \Delta t_n}$, in which α is the correction factor, $c_0 = 1$ is the tracer injection concentration, and $\Delta t' = 1$ seconds is the injection time.

The m -strand stagnant zone ratio ($\frac{V_{d,m}}{V}$) and the overall stagnant zone ($\frac{V_d}{V}$) of the tundish were calculated as follows^[22]:

$$\frac{V_{d,m}}{V} = 1 - \theta_c - \frac{1}{E_{m,\max}} (1 - \theta_{c,m}) \quad [12]$$

$$\frac{V_d}{V} = \frac{1}{N} \sum_{m=1}^N \frac{V_{d,m}}{V}, \quad [13]$$

where $\theta_c = \int_0^2 E_m(\theta) d\theta$, $\theta_{c,m} = \int_0^2 e^{-\theta} d\theta$, and $E_{m,\max}$ is the maximum tracer concentration of the m strand.

Table II. Physical Simulation Parameters

Parameters	Value
Working Height of Tundish	340 mm
Diameter of the Ladle Shroud	64/3 mm
Diameter of the Outlet	10 mm
Submergence Depth of Ladle Shroud	100 mm
Distance Between Two Outlets	600 mm

C. Physical Water Simulations

Physical water simulation tests verify the accuracy of mathematical models and visually record the flow state in the tundish. The geometric parameters of the water simulation model were determined according to the dimensions in Figure 1(a) and Table I and the similarity ratio of 1/3, as shown in Table II. A physical model of the tundish was made using plexiglass, as shown in Figure 2. In the physical experiment, water was used instead of molten steel, and saturated KCl solution (50 mL) was used as a conductivity test tracer. The flow rate at each outlet was set at 3.6 L/min. Data on tracer concentration over time were collected by a conductivity analyzer. The data collection time is 6000 seconds. Potassium permanganate solution was used to show the flow trajectory within the tundish. For the accuracy of the conductivity meter results, the determination of the RTD curve and the recording of the flow trajectory were performed separately.

D. Model accuracy validation

The accuracy of the mathematical model is mainly verified by physical water simulation experiments. Figure 3 illustrates a comparison between the tundish strand 2 RTD curves obtained by the two methods, where the physical simulation was repeated twice. The characteristics of the RTD curves in Figure 3 are similar, and they are each in the bimodal state. Moreover, the stagnant zone proportions, calculated by the RTD stagnant zone theoretical model, are 22.92, 23.80, and 22.19 pct, and the maximum error of both simulation methods is 0.88 pct. Furthermore, Figure 4 shows the flow trajectory of the prototype tundish obtained by the two simulation methods, which shows good agreement. The results demonstrate that the mathematical model solution can serve as the foundation for optimization analysis. Physical parameters, such as the density and viscosity, of molten steel changed during the smelting process and were not taken into account in the simulation, which was the source of errors in the model.

E. Industrial Trials and Analysis Methods

Based on the production plan for 42CrMo4 alloy structural steel [0.42 C, 0.23 Si, 0.61 Mn, 1.0 Cr, 0.17 Mo, 0.08 P, 0.003 S, and balanced Fe (wt pct)], the process was monitored and sampled at the continuous

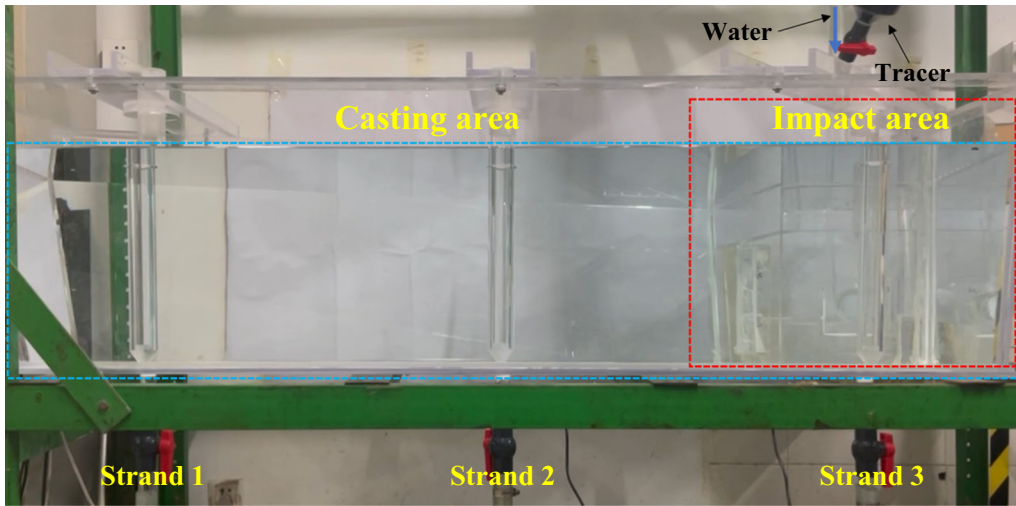


Fig. 2—Tundish physical water simulation experimental device.

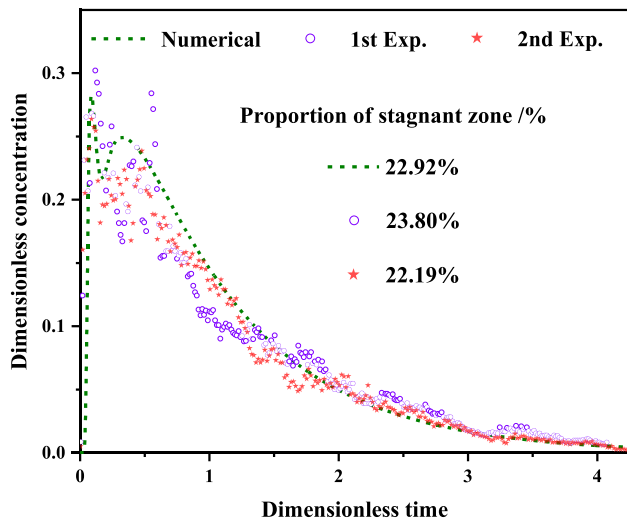


Fig. 3—Verification of mathematical model accuracy.

casting line in the steel plant. To accurately assess the inclusion content, composition, and morphology in the tundish production process, samples were collected from strand 1 and strand 3. Billet samples were collected at the casting line, corresponding to the respective flow times. The samples were analyzed using different tests, as described in Figure 5. A 10-mm-sided cube specimen was extracted from the racket sample. Subsequently, SEM-EDS and ASPEX were used to investigate the content, composition, and morphology of inclusions of 42CrMo4 alloy structural steel in the tundish after grinding and polishing. To determine the total mass of large inclusions in the casting billet, the sample electrolyzing method was employed. This technique allows the exact content of oversized inclusion particles in the billet to be determined and their three-dimensional topography to be visualized.

F. Two-Step Tundish Optimization Scheme Design

Figure 6 illustrates the water simulation flow field and mathematical simulation RTD curve for the three strands of the tundish prototype. The structure of the prototype tundish was seriously flawed. As a result, molten steel flowed directly into strand 2 and strand 3 through the deflector hole in the retaining wall of the impact zone. The rapid peak of tracer concentration on the RTD curve confirms this short-circuit flow phenomenon.^[25] The flow was concentrated in the horizontal direction, the vertical flow relies on convection–diffusion, and the tundish was insufficiently supplied at the far end. The phenomenon of proximal short-circuit flow is obvious, and the phenomenon of flow stratification is serious.

The first step is to optimize and enlarge the tundish impact zone to shorten the distance between the deflector jet and the remote end in the physical structure and to promote the remote flow supply. This step explores the scheme of four sets of different impact zone volumes. The subsequent step of optimization includes the following: according to the simulation results of the first step, three sets of tests were designed to adjust the structural parameters of the basic flow control components. These three sets of tests were designed to solve the remaining problems after impact zone optimization. G1 adjusts the aperture (D_h) values of the deflector holes on retaining walls W1 and W2. G2 identifies the most suitable inclination angle (A_h -W1) of the deflector hole on retaining wall W1, and the optimal parameter for G3 was determined for the distance Z_d between the deflector hole on retaining wall W2 and the wall. The design for the two-step scheme is shown in Table III.

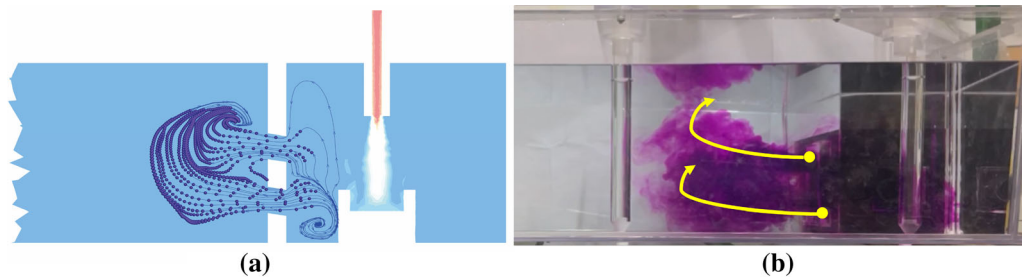


Fig. 4—Flow field of plane I of the tundish prototype section: (a) mathematical simulation and (b) water simulation.

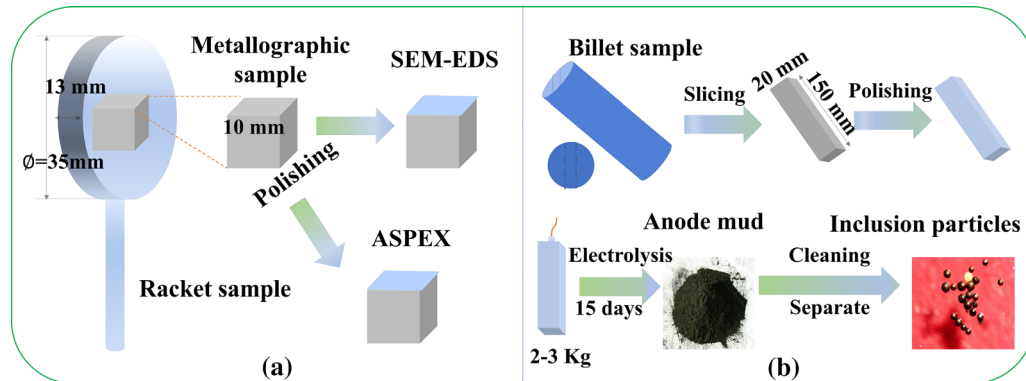


Fig. 5—Experimental characterization method: (a) racket sample and (b) billet sample.

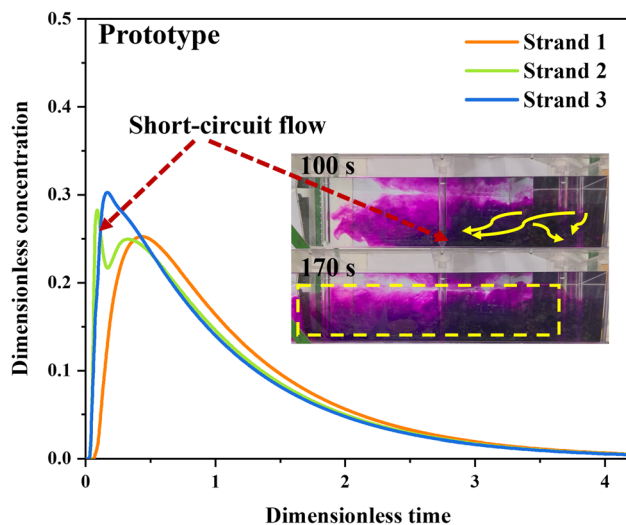


Fig. 6—Flow field information about the physical water simulation of the tundish prototype.

III. RESULTS AND DISCUSSION

A. Effects of Impact Zone Volume on Stagnant Zone Distribution and Proportion

The extremely low-speed region in the tundish is defined as a stagnant zone, which is not conducive to the mutual transport of components and the removal of inclusions,^[26] with a speed cutoff value of 0.005 m/s in this study. Figure 7(a) shows that the low-speed region of the tundish prototype flow field is mainly distributed

in the casting area, and this phenomenon is relatively pronounced near the far flow end. The flow lines surrounding the region validate the origin of the low-speed zone in the tundish, which may be regarded as a stagnant zone prompted by sluggish flow and the absence of molten steel renewal. As shown in Figures 7(b) through (e), we simulated the tundish model by varying the impact zone-to-tundish volume ratio. Relative to the prototype, increasing the proportion of the impact zone volume decreases the number of stagnant zones. The position of the stagnant zone changes accordingly, and the dispersion of remote low-speed regions is mitigated. Figure 7(d) illustrates the distribution of the stagnant zone when the impact zone volume is 19.3 pct. The stagnant zone was eliminated in the distal and lower regions but not highly positively affected in the upper region. Figure 8 shows the proportion of the stagnant zone calculated by the theoretical calculation model of the stagnant zone, which has a similar trend to Figure 7. When the impact zone continues to expand, the impact effect of the impact zone is weakened, the effect on the distal jet is correspondingly reduced, and this positive effect is reduced. Figure 9 illustrates the impacts of different volume proportions of the impact zone on the temperature distribution along the longitudinal section of the outlet in the casting zone. The expansion of the impact zone volume increases the temperature at the distal end. The positive effect of reasonable expansion of the impact zone, which includes the provision of high-temperature fluid for the upper layer, is reflected in the

Table III. Two-Step Method Tundish Optimization Plan

Optimization Step	Case	Structural Parameters		
		Proportion of Impact Zone Volume/Pct	Basic flow Control Components	Research Objectives
Step I	Prototype	13.9 pct	$D_h = 150$ mm	shorten the distance between the beginning and end of the jet
	F1	15.8 pct	$A_h = 10$ deg	
	F2	17.6 pct	$Z_d = 370$ mm	
	F3	19.3 pct		
	F4	20.9 pct		
Step II	G1	19.3 pct	$D_h = 125/100$ mm	cooperate to solve the remaining problems after the volume optimization of the impact zone
	G2		$A_h-W1 = 15/20/25$ deg	
	G3		$Z_d = 420/470$ mm	

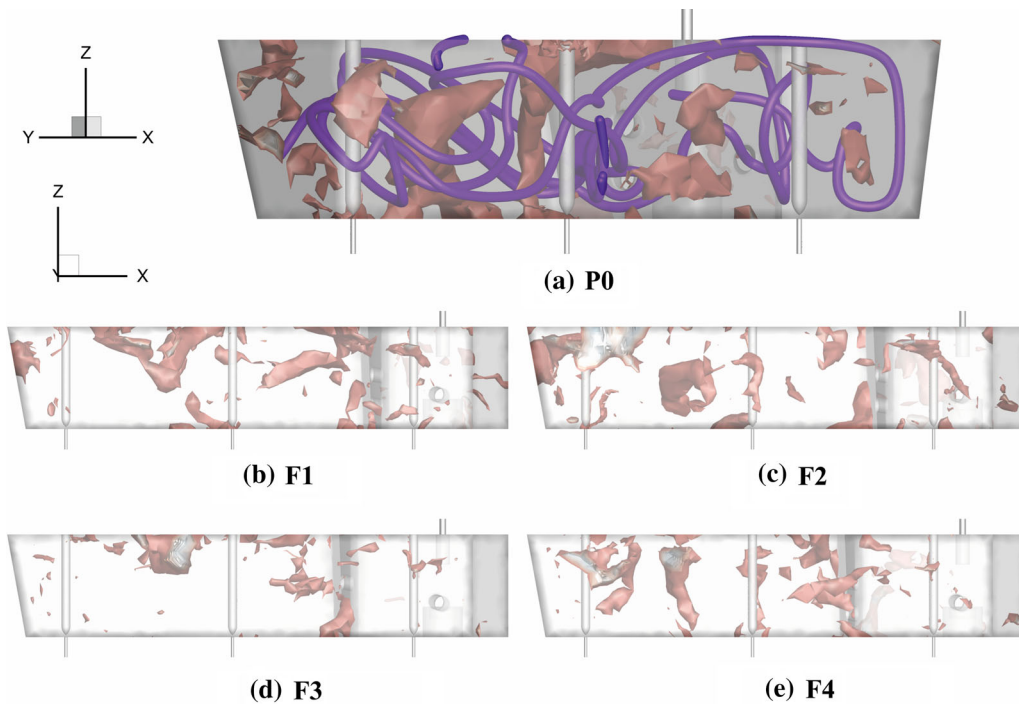


Fig. 7—Effect of impact zone volume on the distribution of the tundish stagnant zone: (a) P0, (b) F1, (c) F2, (d) F3, and (e) F4.

distribution of the high-temperature zone. This effect optimizes the upper and distal flow states, increasing the uniformity of flow field distribution.

B. Tundish Metallurgical Performance Optimized by the Two-Step Method

When the volume of the impact zone is 19.3 pct, it effectively mitigates the limited slow flow in the upper and distal layers. Figure 10(a) depicts the RTD curve of F3, and the short-circuit phenomenon is still severe relative to strand 2 of the prototype. This phenomenon impedes the elimination of inclusions due to insufficient flow time.^[27] The experiment shows that the molten steel jet from the deflector hole on retaining wall W2 is located between strand 2 and strand 3, which may be an

important reason for this severe short-circuit flow. Moreover, Figure 7(d) indicates that enlarging the impact zone volume is insufficient for fully managing the delamination phenomenon. In addition, the plane *I* cross-sectional flow field of the tundish prototype in Figure 4 shows that the inclination angle and opening parameters of the deflection hole on the retaining wall W1 are important factors influencing the molten steel jet. Therefore, it is essential to regulate the structural parameters of the basic flow control components. The specific arrangement of the G1, G2, and G3 groups according to the experiment plan is shown in Table 3.

The structural parameters of the optimized basic flow control assembly were finally obtained by comparing the comprehensive indexes of the three sets of tests, including the stagnant zone content, flow field, and

temperature field distribution information. The comparison of simulation data for cases with different structural parameters is shown in Figure 10. The results confirmed that reducing the guide hole size and increasing the inclination angle of the deflector holes can promote the flow at the distal end. As shown in Figure 10(c), the steel shows a better-mixed flow in the tundish, while the stratified flow of the other schemes is still significant (marked in Figures 10(a), (b) and (d)). The final optimized structural parameters are shown in Figure 11(b). The structural parameters for optimizing the tundish include the impact zone volume accounting for 19.3 pct of the tundish volume, a 100 mm diameter for the deflector hole on all retaining walls, and a 20 deg inclination angle for the deflector hole on retaining wall W1. The inclination angle of the deflector on the

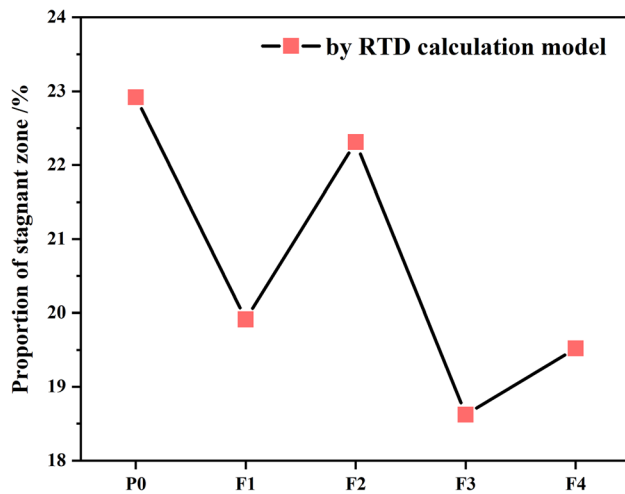


Fig. 8—Influence of impact zone volume on the proportion of the stagnant zone.

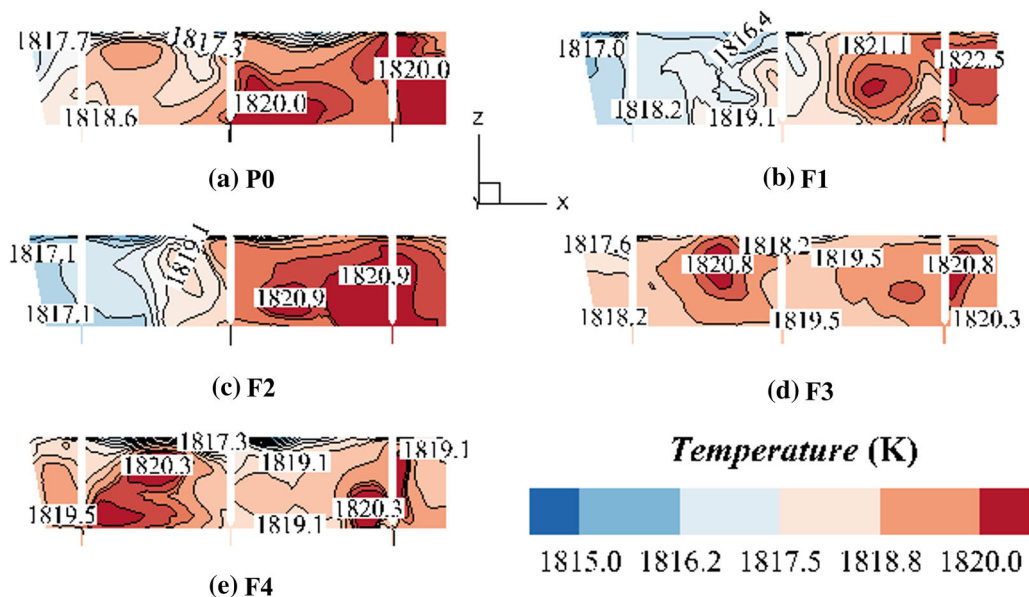


Fig. 9—Effect of impact zone volume on the temperature distributions of longitudinal section of strands: (a) P0, (b) F1, (c) F2, (d) F3, and (e) F4.

retaining wall W2 is consistent with the tundish prototype. The distance Z_d is 420 mm. Figure 11(b) shows the RTD curve of the optimized tundish with a great modification relative to F3. The reduction in the peak concentration and the flattening of the curve of strand 2 show that the serious short-circuit flow phenomenon is eliminated, and the consistency of the three strands is greatly improved.

Figure 12 shows the tundish prototype and the optimized flow field diagram, and the expansion of the impact zone volume prolongs the time for water to flow from the deflector. However, at 40 seconds, the tracer under both models approaches the same position, indicating that the optimized model has a strong jet capacity and that this positive trend is persistent. Fluid stratification is almost nonexistent in the optimized model, indicating that the uniformity of material exchange is greatly improved at various places in the middle. Figure 13 shows a comparison of water simulation RTD curves before and after tundish optimization. The optimized structure greatly reduces the peak concentration of the tracer. The improved consistency of the monitoring curve for each outlet tracer verifies the improved uniformity of the flow field in Figure 12. Relative to the magnitude of peak concentration reduction, the optimization of uniformity is less effective for strands 1 and 3, which corresponds to the results of the numerical simulations. In addition, the homogeneity of the tracer dissolution leads to some differences. This phenomenon establishes the basis for the clean production of high-quality special steels.

C. Distribution and Removal of Inclusions

We explored the compositions and shapes of inclusions in the casting zone, as illustrated in Figures 14 and 15. The principal inclusions present in the 42CrMo4 alloy structural steel during the tundish smelting period

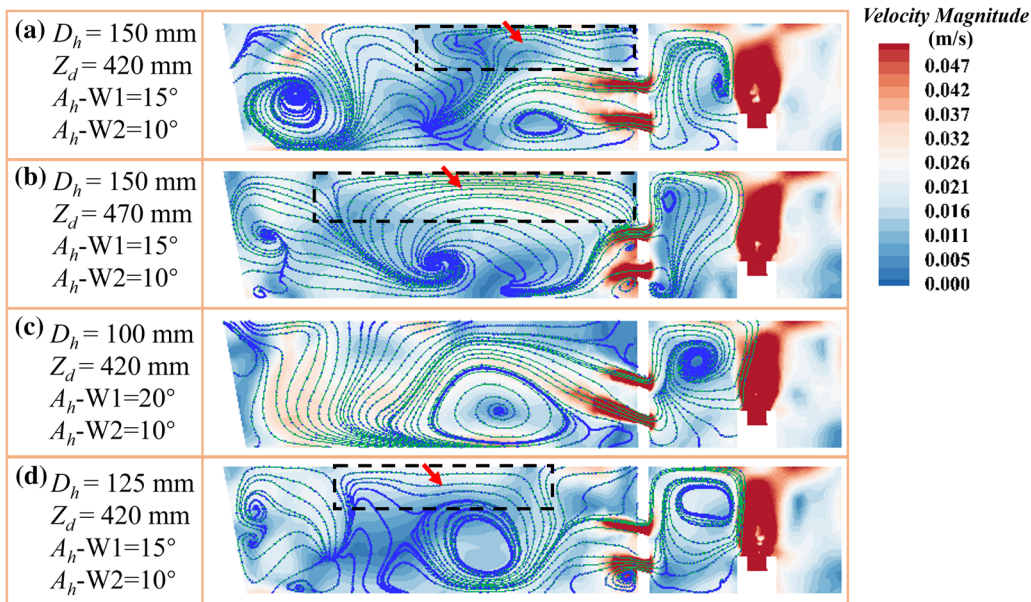


Fig. 10—Velocity-flow field of cross-sectional plane *I* with different structural parameters.

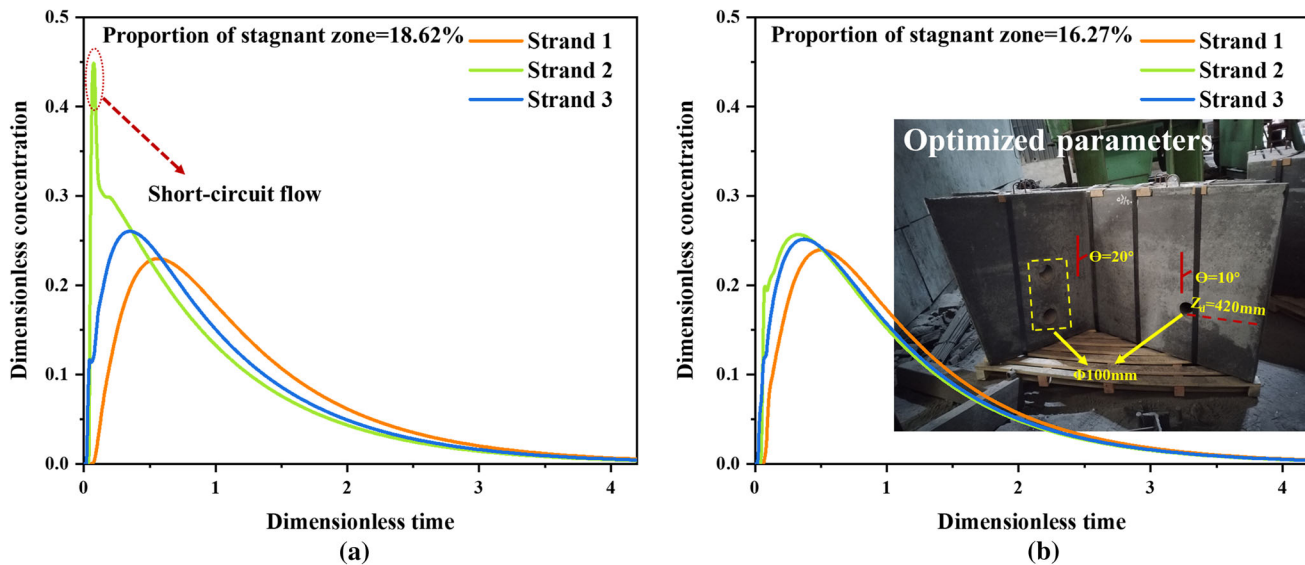


Fig. 11—Comparison of RTD curves: (a) F3 and (b) optimization.

are Al_2O_3 , CaS , CaO and composites of these inclusions, with a diameters in the range of 1–10 μm . The state of inclusions in the smelting process plays an important role in the production of steel purification,^[3] and the liquid phase distribution of Al_2O_3 - CaS - CaO at 1873 K was calculated by FactSage 8.2 software, showing that the average composition of inclusions in the production of 42CrMo4 is not in the corresponding liquid phase region and is mostly solid in the casting process of the tundish. Therefore, as the final liquid reactor, it is essential to consider the impact of the tundish inclusion removal performance on the clean production of 42CrMo4. Addressing these issues is crucial. There are great inaccuracies in the densities of inclusions from 2D and 3D perspectives^[28,29] due to sampling timing,

postobservation, and human subjective factors. The inclusion particles separated from the steel matrix were obtained by electrolyzing the billets of different casting heats corresponding to the same flow times before and after tundish optimization. The three-dimensional morphologies of the inclusions were observed, and the large inclusions in the steel were weighed and analyzed.

Figure 16(a) shows a $\times 20$ magnification of the inclusion particles under an optical microscope. The inclusions are mainly spherical and very large due to the size screening of the inclusion particles after electrolysis. The results of the inclusion particle field emission electron microscopy in Figure 16(b) correspond to the inclusion composition distribution in Figure 14. The TMIs corresponding to strands 1 and 3 in the first heat

casting process of the tundish are reduced from 2.76 and 3.03 mg/10 kg to 1.06 and 1.68 mg/10 kg in the prototype tundish, respectively, and the intermediate heat is reduced from 2.46 and 2.52 mg/10 kg to 1.06 and 1.68 mg/10 kg, respectively. The corresponding TMIs of the tail heat are 1.39 and 0.46 mg/10 kg, as shown in Figure 17. In the single-cast period perspective, the TMIs of the distal flow order of the tundish are lower than those of the proximal flow order^[29] because of the long float time. The results of Figure 17 are consistent with this conclusion. Throughout the casting period perspective, the TMIs fluctuate greatly from the casting period to casting. The main manifestation is that the first heat and tail heat are higher than the intermediate heat, which may be caused by unsteady casting processes, such as opening and changing the first heat stage

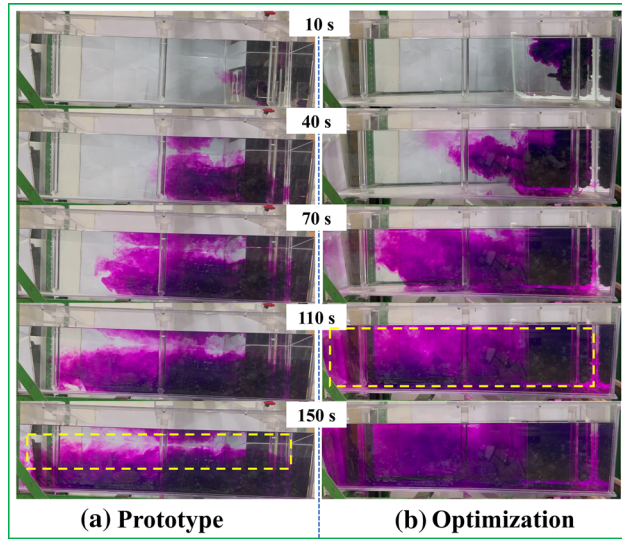
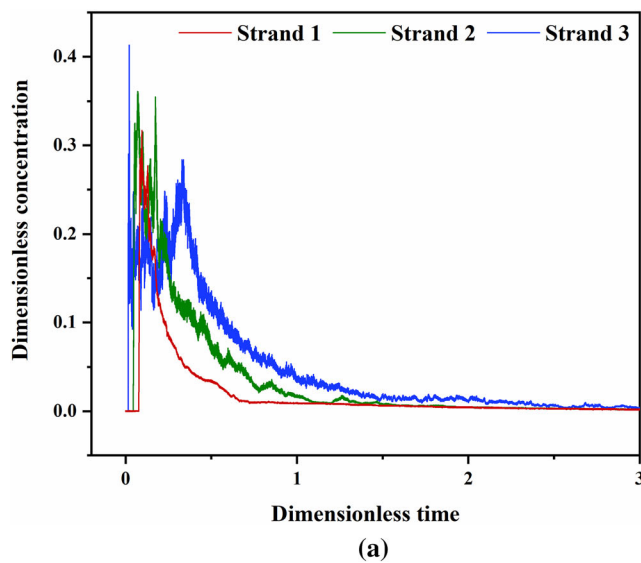


Fig. 12—Flow field information obtained through physical water simulation: (a) prototype and (b) optimization.



and tail heat stage, easily leading to large liquid level fluctuations. As shown by the TMIs of strand 3 in the tail heat in Figure 17, due to unknown and uncontrollable factors, such as on-site sampling and experimental errors, the conclusions from these two perspectives are sometimes not completely in line with the actual situation. A detailed comparison is conducted as follows. In the same casting period, the molten steel in the optimized tundish structure has a long flow trajectory, a relatively long residence time, and sufficient inclusion floating, occurring due to an increase in the difference between the TMIs of distal strand 1 and proximal strand 3 relative to the prototype.

D. Retaining Wall Crack Analysis

Figure 18 is a physical diagram of the tundish before and after use in industrial trials. The retaining wall of the tundish has an important role in stabilizing the flow control process. The optimized tundish structure provides important support in terms of billet cleanliness,

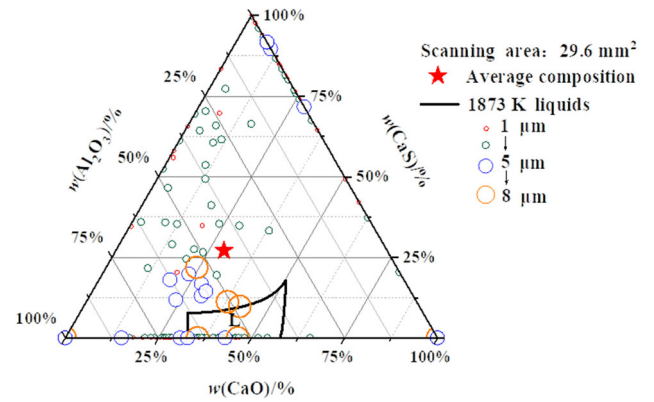


Fig. 14—Distribution of inclusions in the tundish at the beginning of casting.

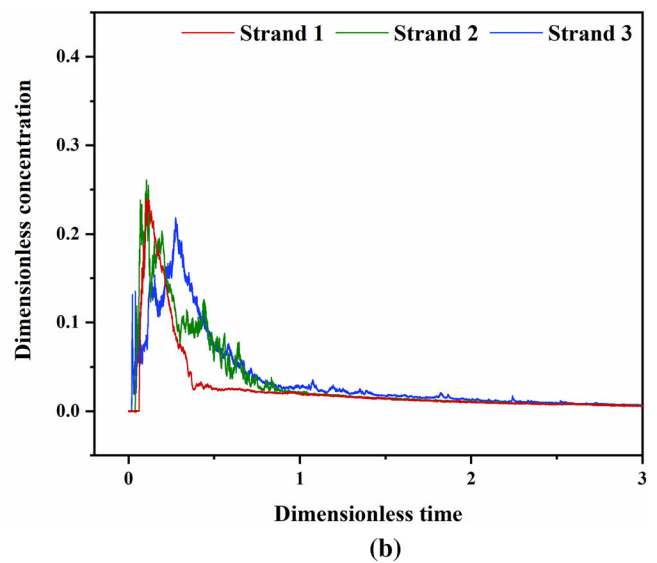


Fig. 13—Comparison of water simulation RTD curves: (a) prototype and (b) optimization.

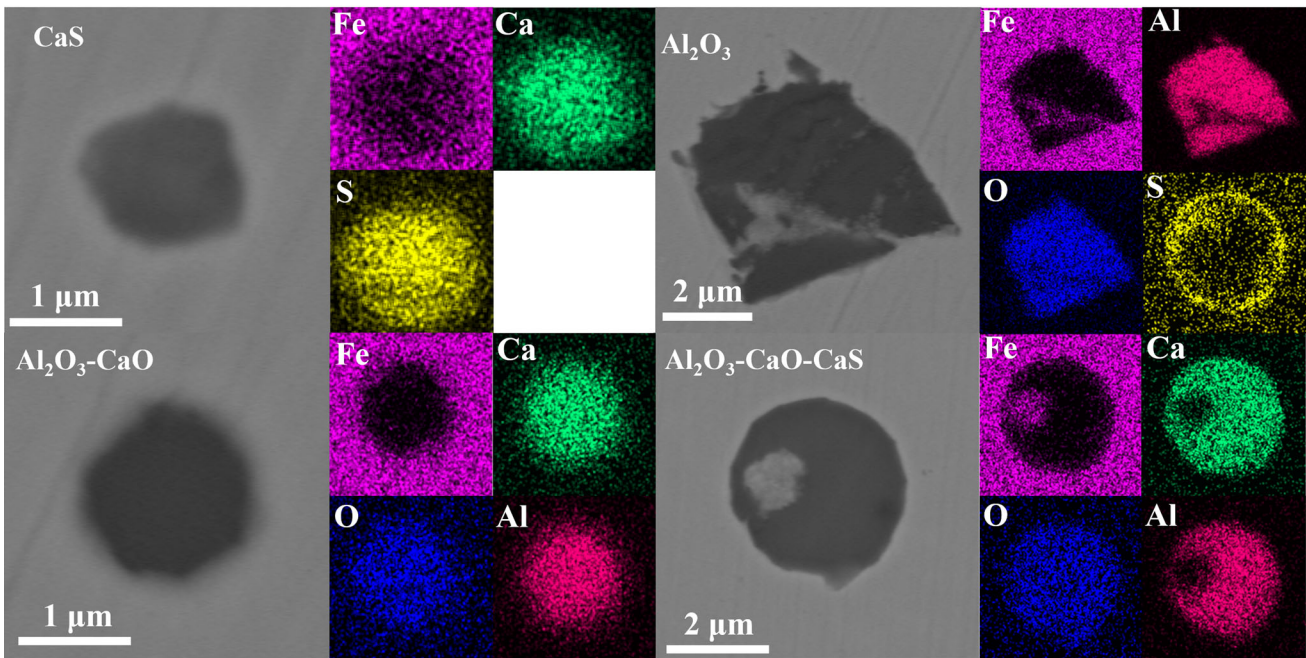


Fig. 15—Morphologies of typical inclusions.

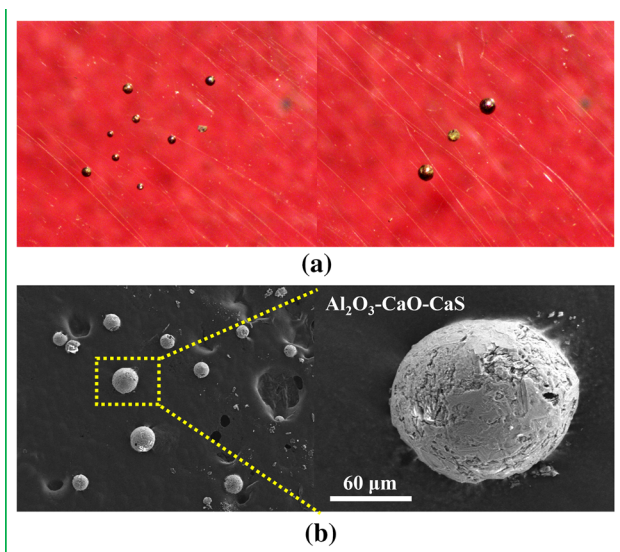


Fig. 16—Three-dimensional morphologies of large inclusions: (a) optical microscopy and (b) SEM.

but after the continuous casting of 19 heats, the retaining walls W1 and W2 have different degrees of cracking, as shown in Figure 18(b). Figure 19 shows the cloud map of the wall shear stress(WSS) and turbulent kinetic energy(TKE) distribution of the retaining walls after optimization, and it is intuitively shown that the cracks in retaining walls W1 and W2 appear in the concentrated distribution area. The cloud map results show that retaining wall W2 is subjected to relatively strong molten steel impact, and the risk of crack occurrence is great.

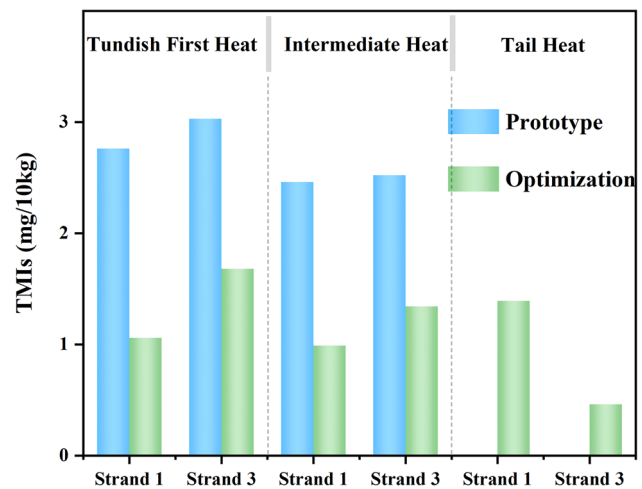


Fig. 17—Electrolytic weighing results at different casting periods of billets.

In future work, the structural parameters of the retaining wall need to be further improved to reduce the impact of molten steel on the retaining wall to cooperate with the strong inclusion removal ability and comprehensively improve the service life of the tundish.

IV. CONCLUSIONS

A two-step optimization method based on the volume of the tundish impact zone was proposed and implemented during the production of 42CrMo4 alloy structural steel. We investigated the removal efficiencies of inclusions and the causes behind retaining wall cracks.

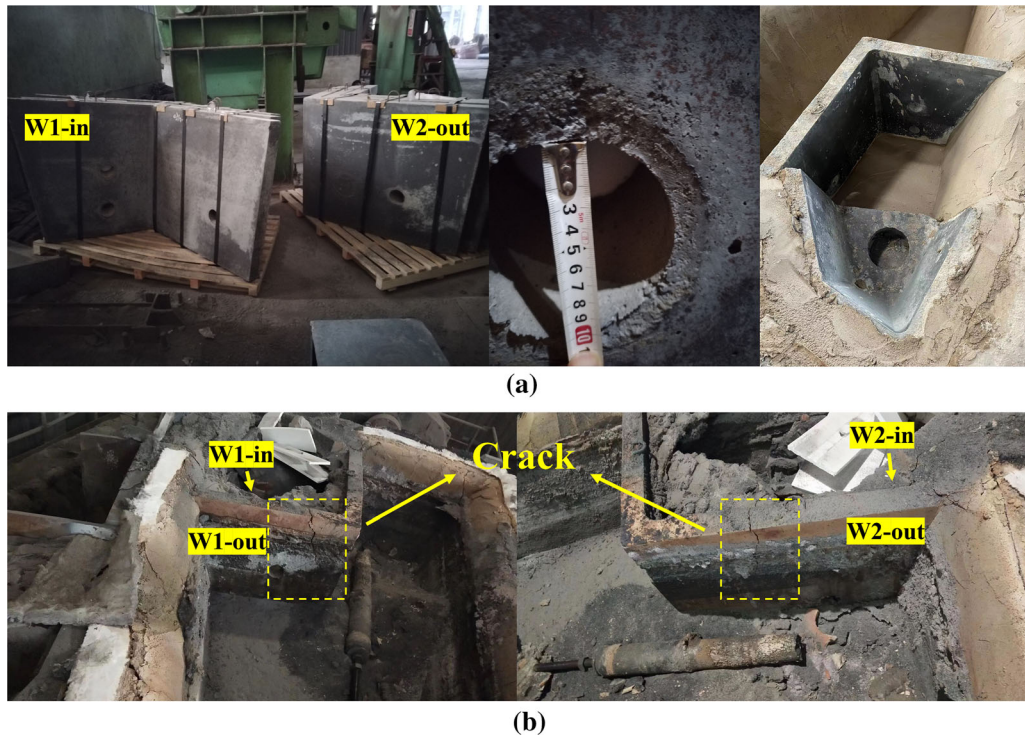


Fig. 18—Physical diagram of the tundish for industrial trials: (a) before and (b) after.

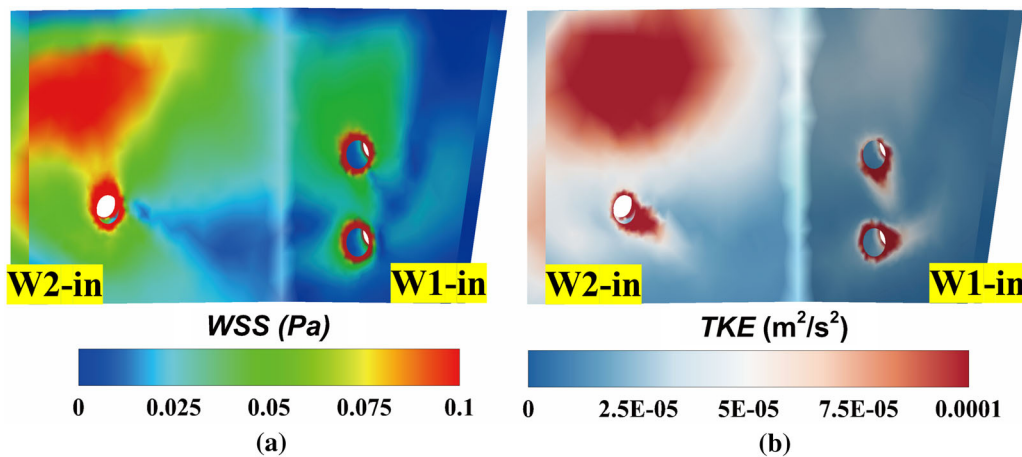


Fig. 19—Distribution of the (a) wall shear stress and (b) turbulent kinetic energy on the wall surface.

- (1) The results of numerical and physical simulations indicated that the volume fraction of the tundish impact zone significantly affected the flow state, with a volume fraction of 19.3 pct identified as the optimal value. Subsequent optimization of the basic flow control devices determined the optimal parameters of the tundish structure.
- (2) The inclusion content in the casting billet was significantly reduced. Industrial experiments identified the primary inclusions that occurred during tundish casting as Al_2O_3 , CaS , CaO , and their composite inclusions, with diameters in the range of 1–10 μm . An electrolytic process was used to quantitatively evaluate the effectiveness of the tundish in removing

large inclusions. The TMIs in intermediate heat strands 1 and 3 showed a decrease from 2.46 mg/10 kg and 2.52 mg/10 kg to 1.06 mg/10 kg and 1.68 mg/10 kg, respectively.

- (3) The numerical simulations and industrial trials demonstrated that cracks appeared in the upper section of the retaining wall during tundish continuous casting. The simulations confirmed that the constant impact of molten steel created cracks and that the W2 of the retaining wall had a relatively high risk of cracking. These findings suggested a new approach for future long-term tundish research.

ACKNOWLEDGMENTS

This work was supported by the National Natural Science Foundation of China (Grant Nos. 52374320, 52104318, and 52074030).

CONFLICT OF INTEREST

The authors declare that they have no conflicts of interest.

REFERENCES

1. Q. Wang, Y. Liu, A. Huang, W. Yan, H.Z. Gu, and G.Q. Li: *Metall Mater. Trans. B*, 2019, vol. 51B(1), pp. 276–92.
2. V.K. Gupta, P.K. Jha, and P.K. Jain: *J. Manuf. Process.*, 2022, vol. 83, pp. 27–39.
3. T. Qiao, G. Cheng, Y. Huang, Y. Li, Y. Zhang, and Z. Li: *Metals*, 2022, vol. 12(9), p. 1505.
4. Y. Sahai: *Metall Mater. Trans. B*, 2016, vol. 47B(4), pp. 2095–06.
5. F. He, H. Wang, and Z.Z. Hu: *ISIJ Int.*, 2019, vol. 59(7), pp. 1250–58.
6. C. Yao, M. Wang, M.X. Pan, and Y.P. Bao: *J. Iron Steel Res. Int.*, 2021, vol. 28(9), pp. 1114–24.
7. D. Chen, X. Xie, M. Long, M. Zhang, L.L. Zhang, and Q. Liao: *Metall. Mater. Trans. B*, 2013, vol. 45B(2), pp. 392–98.
8. X.Y. Wang, D.T. Zhao, S.T. Qiu, and Z.S. Zou: *ISIJ Int.*, 2017, vol. 57(11), pp. 1990–99.
9. S. Yang, Z. Che, C. Liu, W. Liu, J. Li, X. Cheng, and X. Li: *Corros. Sci.*, 2023, vol. 212, p. 110970.
10. M.J.K. Lodhi, A.D. Iams, A.E. Sikor, and T.A. Palmer: *Corros. Sci.*, 2022, vol. 203, p. 110354.
11. K. Gillner, M. Henrich, and S. Münstermann: *Int. J. Fatigue*, 2018, vol. 111, pp. 70–80.
12. Y. Hu, W. Chen, C. Wan, F. Wang, and H. Han: *Metall Mater. Trans. B*, 2018, vol. 49B(2), pp. 569–80.
13. P. Wang, P. Zhang, B. Wang, Y. Zhu, Z. Xu, and Z. Zhang: *J. Mater. Sci. Technol.*, 2023, vol. 154, pp. 114–28.
14. D.G. Zhao, Y.F. Wang, M. Gao, and S.H. Wang: *Ironmak. Steelmak.*, 2017, vol. 46(3), pp. 235–45.
15. C. Yao, M. Wang, H. Zhu, L. Xing, and Y. Bao: *Metall Mater. Trans. B*, 2023, vol. 54B(3), pp. 1144–58.
16. S. Garcia-Hernández, J.D.J. Barreto, J.A. Ramos-Banderas, and G. Solorio-Diaz: *Steel Res. Int.*, 2010, vol. 81(6), pp. 453–60.
17. W. Liu, S.F. Yang, J.S. Li, F. Wang and H. B. Yang: *J. Iron Steel Res. Int.*, 2019, vol.26(11), pp.1147–53.
18. C. Ding, H. Lei, H. Zhang, M. Xu, Y. Zhao, and Q. Li: *J Mater. Res. Technol.*, 2023, vol. 23, pp. 5400–12.
19. W. Liu, J. Liu, H. Zhao, S. Yang, and J. Li: *Metall Mater. Trans. B*, 2021, vol. 52B(4), pp. 2430–40.
20. Y. Sahai and T. Emi: *ISIJ Int.*, 1996, vol. 36(6), pp. 667–72.
21. B. Yang, X. Liao, K. Liu, C. Zhao, and P. Han: *Jom-US*, 2022, vol. 74(5), pp. 2129–38.
22. X. Su, Y. Ji, J. Liu, Y. He, S. Shen and H. Cui: *Steel Res Int.*, 2018, vol.89(12), pp. 1885.
23. D.B. Spalding: *Numerical Prediction of Flow, Heat Transfer, Turbulence and Combustion*. Pergamon,1st ed., CRC Press, New York,1983, pp.96–116.
24. H.W. Pan and S.S. Cheng: *Chin. J. Eng. Des. Eng. Des.*, 2009, vol. 31(7), pp. 815–20.
25. L. Zhong, B. Li, Y. Zhu, R. Wang, W. Wang, and X. Zhang: *ISIJ Int.*, 2007, vol. 47(1), pp. 88–94.
26. Q. Zhang, G. Xu, and K. Iwai: *ISIJ Int.*, 2022, vol. 62(1), pp. 56–63.
27. Q. Fang, H. Zhang, R. Luo, C. Liu, Y. Wang, H. Ni, and J. Mater: *Res. Technol.*, 2020, vol. 9(1), pp. 347–63.
28. L. Zhang, B. Rietow, B.G. Thomas, and K. Eakin: *ISIJ Int.*, 2006, vol. 46(5), pp. 670–79.
29. H. Ling, L. Zhang, and H. Li: *Metall Mater. Trans. B*, 2016, vol. 47B(5), pp. 2991–3012.

Publisher's Note Springer Nature remains neutral with regard to jurisdictional claims in published maps and institutional affiliations.

Springer Nature or its licensor (e.g. a society or other partner) holds exclusive rights to this article under a publishing agreement with the author(s) or other rightsholder(s); author self-archiving of the accepted manuscript version of this article is solely governed by the terms of such publishing agreement and applicable law.